LETTERS

Upside-down differentiation and generation of a 'primordial' lower mantle

Cin-Ty A. Lee[1], Peter Luffi[1], Tobias Höink[1], Jie Li[2], Rajdeep Dasgupta[1] & John Hernlund[3]

Except for the first 50–100 million years or so of the Earth's history, when most of the mantle may have been subjected to melting, the differentiation of Earth's silicate mantle has been controlled by solid-state convection[1]. As the mantle upwells and decompresses across its solidus, it partially melts. These low-density melts rise to the surface and form the continental and oceanic crusts, driving the differentiation of the silicate part of the Earth. Because many trace elements, such as heat-producing U, Th and K, as well as the noble gases, preferentially partition into melts (here referred to as incompatible elements), melt extraction concentrates these elements into the crust (or atmosphere in the case of noble gases), where nearly half of the Earth's budget of these elements now resides[2]. In contrast, the upper mantle, as sampled by mid-ocean ridge basalts, is highly depleted in incompatible elements, suggesting a complementary relationship with the crust. Mass balance arguments require that the other half of these incompatible elements be hidden in the Earth's interior. Hypotheses abound for the origin of this hidden reservoir[3–6]. The most widely held view has been that this hidden reservoir represents primordial material never processed by melting or degassing. Here, we suggest that a necessary by-product of whole-mantle convection during the Earth's first billion years is deep and hot melting, resulting in the generation of dense liquids that crystallized and sank into the lower mantle. These sunken lithologies would have 'primordial' chemical signatures despite a non-primordial origin.

The prevailing view of a primordial lower mantle reservoir is driven largely by the isotopic signatures of noble gases in mid-ocean ridge basalts (MORBs) and ocean island basalts. MORBs, which tap the upper mantle, are depleted in primordial noble gas components, whereas ocean island basalts are enriched (for example, high ^{3}He/^{4}He) and are therefore thought to indicate the presence of undegassed primitive reservoirs deep within Earth's interior[7,8]. These observations have led to the paradigm of layered mantle convection for the Earth: that only the upper 660 km of the mantle has differentiated, whereas the lower mantle (deeper than 660 km) has remained unprocessed, thus retaining its primordial and undegassed signatures. However, preservation of a primordial lower mantle is at odds with seismic evidence that some slabs descend to the core–mantle boundary, which suggests whole-mantle convection[9]. To reconcile this discrepancy, Fe-rich chemical boundary layers formed by sinking of Hadean (the first 100 million years of the Earth's history) magma ocean liquids or by subduction of oceanic crust have been suggested as possible alternatives to a primordial layer[1,10–12], but these scenarios are unlikely to preserve primordial noble gas signatures, because any magma that rises to the Earth's surface will have degassed.
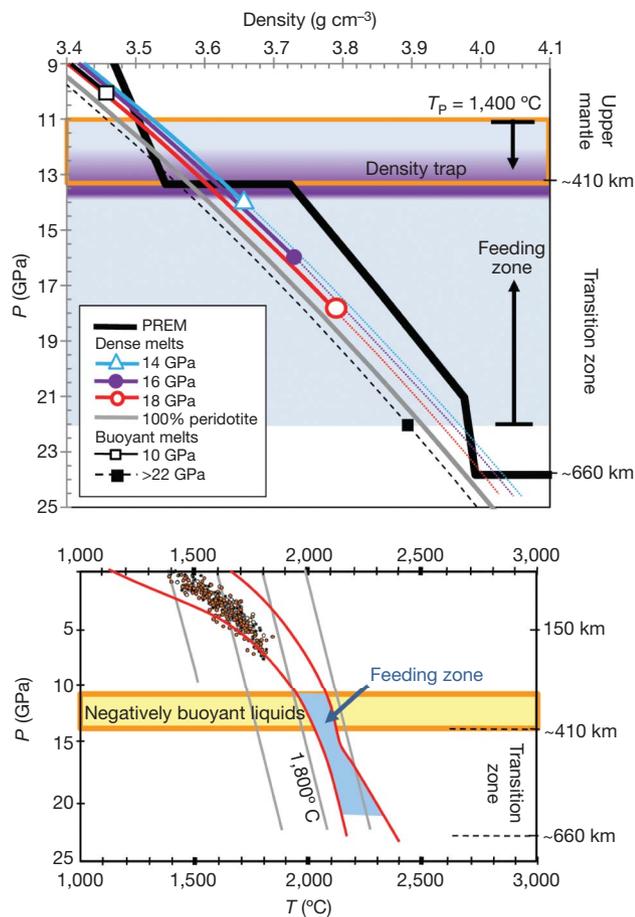
A very different story would emerge if liquids sink instead of rise. Under certain high-pressure conditions, it has been suggested that peridotite partial melts may be more dense than solid peridotite because such liquids are Fe-rich and more compressible than solids[13–15]. Partial melts of peridotite at 9–23 GPa (270–660 km) are ultramafic (MgO > 25 wt%) and more enriched in Fe than their low-pressure equivalents because Fe is favoured in liquids with increasing temperature and pressure[16]. Figure 1a compares the densities of these melts calculated for a mantle potential temperature of 1,400 °C (representative of modern mantle[15,17,18]; see Methods) with the present-day mantle density structure as represented by the Preliminary Reference Earth Model (PREM)[19]. At pressures greater than 14 GPa (that is, deeper than the 410 km discontinuity) and less than ~10 GPa (<300 km), liquids are less dense than PREM and hence rise (these results are consistent with ref. 20). However, within the upper mantle (<~410 km) there is a depth interval of ≤100 km (~10–14 GPa) just above the transition zone (14–24 GPa; 410–660 km), wherein partial melts of peridotite are denser than PREM. This density contrast is probably independent of temperature because the thermal expansion coefficients of these liquids and peridotite are similar. Of particular interest is that melts generated within the transition zone (for example, the 14 and 18 GPa melt compositions in Fig. 1), while positively buoyant in their source regions, are denser than PREM in the 10–14 GPa interval. In contrast, near-solidus melts formed at pressures >22 GPa in the lowermost transition zone and the upper part of the lower mantle never become negatively buoyant because residual ferropericlase suppresses the Fe content in the melt (Fig. 1a).

Provided the Earth's thermal state was sufficient for deep and hot melting, we envision the region around the upper mantle–transition zone (UM–TZ) interface (~14 GPa) as a 'density trap' (Fig. 2), in which buoyant melts rising from the transition zone stall and in which dense melts sinking from the 10–14 GPa interval in the upper mantle accumulate. We envision the entire interval of dense melt generation (~10–22 GPa) as the 'feeding zone' of dense melts that converge to the density trap. These accumulated liquids will eventually crystallize, either by pressure-induced crystallization (for those liquids that sank) or by cooling as such material is diverted away from upwelling centres (Fig. 2). This crystallized product manifests itself in the form of refertilized solid mantle that is richer in Fe and hence denser than unadulterated peridotitic mantle. This Fe-rich hybrid rock should then sink into the lower mantle, eventually settling at the core–mantle boundary to form a Fe-rich chemical boundary layer (Fig. 2).

The minimum potential temperature necessary for generating negatively buoyant melts is defined by the top of the feeding zone (~10 GPa) and corresponds to a potential temperature of ~1,800 °C (Fig. 1b). The maximum permissible potential temperature is determined by the bottom of the feeding zone (~22 GPa) and corresponds to a potential temperature of ~2,000 °C (as determined from the temperature of melting at these depths; Fig. 1b). As shown previously and as outlined in the Methods[21,22], the oldest komatiites (3.5 Gyr) record potential temperatures of ~1,750 °C. If this is representative

[1]Department of Earth Science, MS-126, Rice University, 6100 Main Street, Houston, Texas 77005, USA. [2]Department of Geological Sciences, University of Michigan, Ann Arbor, Michigan 48109-1005, USA. [3]Department of Earth and Planetary Science, University of California, Berkeley, California 94720, USA.

Figure 1 | Conditions for dense melt generation. a, Densities of 10, 14, 16 and 18 GPa near-solidus melts of peridotite, as well as 100% peridotite melt from ref. 16, calculated along a mantle adiabat corresponding to a 1,400 °C potential temperature. Also shown are 22 GPa melts[20] for reference. The thick black line represents the density of mantle from PREM[19]. The horizontal field outlined in orange is the pressure interval (~10–14 GPa) in which liquids are denser than PREM. The blue region is the 'feeding zone' for liquids that eventually become denser than PREM between 10 and 14 GPa. The purple shaded region is a convergence zone ('density trap') in which melts rising from the transition zone stall, and in which melts sinking from the 10–14 GPa interval in the upper mantle accumulate. **b,** The temperature (T) and pressure (P) equilibration of primary komatiitic magmas from the South African, west Australian and Canadian cratons, calculated using the approach of ref. 22 (± 0.2 GPa, ± 40 °C, 2σ). Also shown are the anhydrous solidus and liquidus of peridotite (red lines)[16], and solid mantle adiabats (straight grey lines) for given potential temperatures. The intersection of komatiite P–T data defines the mantle adiabat for generation of komatiites. The blue-shaded region is the P–T field of the feeding zone in **a.** The horizontal shaded region is the P-interval in which melts are denser than PREM.

of global average potential temperatures in the Early Archaean era, such liquids could have formed before ~3.5 Gyr ago. A more precise time window for the formation of Fe-rich hybrid lithologies depends on how long the temperature of the Earth's mantle resided between ~1,800–2,000 °C, but cannot be constrained as long as uncertainties in thermal-history models of the Earth[23–25] remain large. However, for at least some window in Earth's first billion years, melting within

the transition zone and just above the UM–TZ interface must have been a by-product of whole-mantle convection and therefore, generation of Fe-rich hybrid layers, as described here, must have occurred.

Long-term sequestration of these Fe-rich lithologies at the base of the mantle has intriguing geochemical implications. Because incompatible trace elements, including all the volatiles, are partitioned into the melt phase, transport of these crystallized liquids to the lower mantle will give rise to a deep-mantle reservoir preserving primordial relative abundances of incompatible elements. Primordial (U+Th)/He ratios, for example, will then result in primordial (high) time-integrated ^{3}He/^{4}He ratios compared to portions of the mantle that were processed in the shallow mantle and degassed (and hence will have evolved to low ^{3}He/^{4}He ratios; Fig. 3a). This sequestered component would have primordial time-integrated ^{143}Nd/^{144}Nd, ^{87}Sr/^{86}Sr and ^{206}Pb/^{204}Pb because both the parent and daughter elements in these isotope systems are also highly incompatible. Likewise, the high K in this chemical boundary layer would generate radiogenic ^{40}Ar, accounting for some of the Ar presumed to be missing from the atmosphere and mantle.

These features are reminiscent of the 'FOZO'-like geochemical entity, a component in the mantle thought to be ubiquitous in ocean
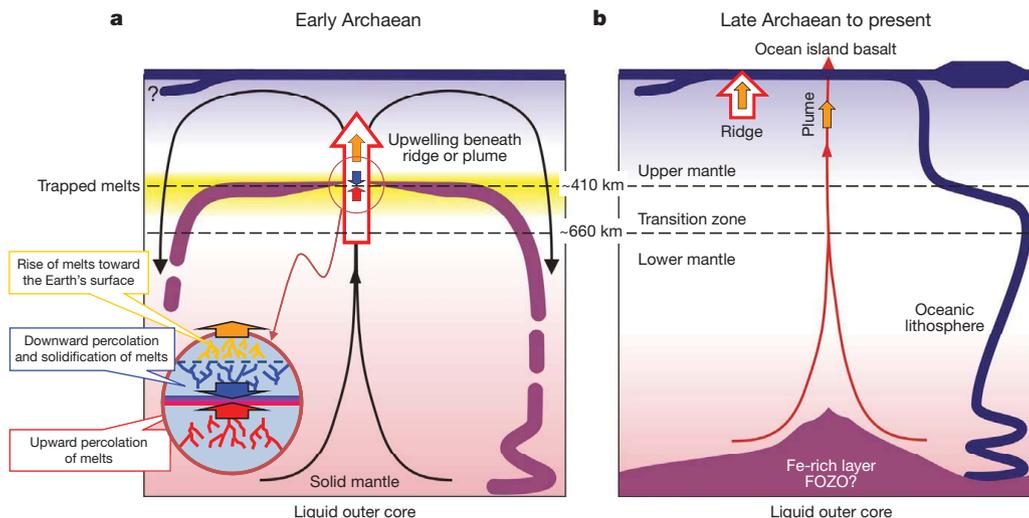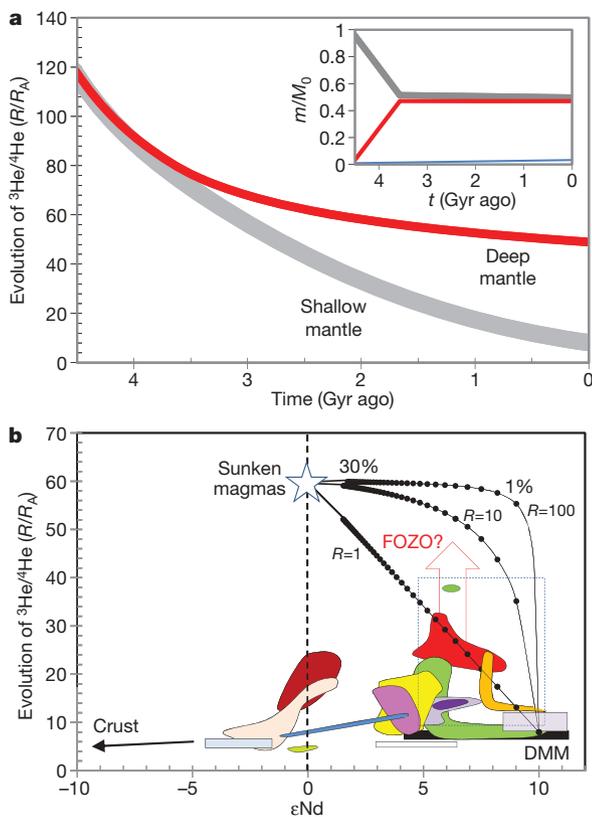

Figure 2 | Melting in the Archaean and modern mantle. a, Early Archaean hot mantle: melts generated in the transition zone and lowermost upper mantle (the feeding zone) accumulate in the density trap at the UM–TZ interface, and upon crystallization, form a dense and refertilized layer. This layer founders or is entrained into the lower mantle by background solid-state convection, resulting in a Fe-rich chemical boundary layer at the bottom of the mantle. This layer is enriched in incompatible elements, noble

gases and heat-producing elements. We note that shallower melting produces low-density liquids (basalts and komatiites), which rise to the surface. **b,** Late Archaean to present cool mantle: melting is restricted to shallow depths where all liquids are buoyant and rise to the surface. Thermal upwellings will entrain primordial-like material from the chemical boundary layer into overlying depleted mantle, generating the 'FOZO' geochemical signature seen in ocean island basalts (see Fig. 3).

Figure 3 | Generation of 'primordial', undegassed lower mantle.
a, Evolution of $^3He/^4He$ (as R/R_A, where R is the isotopic ratio of the reservoir and R_A is that of the present-day atmosphere) in the Earth's silicate reservoirs. Differentiation of the silicate Earth generates continental crust and a deep-mantle reservoir, the latter formed by dense liquids generated during the Earth's first billion years. He, U and Th are highly incompatible and enter the liquid. Dense liquids transport He, U and Th quantitatively to the lower mantle, but differentiation in the uppermost mantle results in unidirectional loss of He to the atmosphere and partial transport of U to the crust (90% of crustal U is assumed to recycle back to the mantle). The rate constants for flow from shallow to deep mantle, shallow mantle to continental crust, and continental crust to shallow mantle are 0.47, 0.55, and 0.545 per Gyr. Deep Fe-rich mantle reservoir does not return to the upper mantle. The inset shows mass proportions (relative to the silicate Earth, m/M_0, where m is mass and M_0 is the mass of the silicate Earth) of the two reservoirs as a function of time. **b**, $^3He/^4He$ versus $^{143}Nd/^{144}Nd$ in epsilon units (1 part in 10^4 deviations from chondrite). Shaded or coloured fields are ocean island ('hotspot') basalt fields[8], the horizontal black bar is DMM (as defined by MORB), the open dotted-outline rectangle is Iceland, FOZO (red arrow) is the hypothesized common component in the mantle source of ocean island basalts[6], and the star is the time-integrated composition of Fe-rich lithologies generated by sinking liquids. Mixing lines are between DMM and 'sunken liquids', using Nd from ref. 32 for DMM and multiplying the Nd concentration of the bulk silicate Earth by five for the sunken liquid (assuming liquids are 20% melts, though the exact value is not critical). Lines correspond to different concentration ratios R of $(He/Nd)_{sunken\ liquid}$ versus $(He/Nd)_{DMM}$. Tick marks are at 1% intervals (and stop at 30%).

island basalts[26]. An unresolved, paradoxical feature of FOZO is that it is enriched in $^3He/^4He$ and hence undegassed. Yet, at the same time, FOZO has a MORB-like or depleted signature in most other radiogenic isotope systems, which suggests processing through the upper mantle and by implication degassing[6,26]. This apparent paradox is exactly what would be expected (Fig. 3b) if the Fe-rich chemical boundary layer were to mix with any mantle (only small amounts, <5%, are needed), such as 'depleted MORB mantle' (DMM) or its ancestral analogue, that has been previously depleted and degassed by shallow mantle processes. Because the He concentration in the chemical boundary layer is much higher than in the degassed DMM, mixing of such material into DMM leads to a substantial increase in $^3He/^4He$ but

to only slight changes in the other radiogenic isotope systems, such as $^{143}Nd/^{144}Nd$, $^{87}Sr/^{86}Sr$, $^{206}Pb/^{204}Pb$ and $^{187}Os/^{188}Os$ (the concentrations of these elements in DMM and the chemical boundary layer are not very different; Fig. 3b). This 'mixture' inherits both the depleted signature of DMM and the undegassed signature of the Fe-rich chemical boundary layer. This is FOZO. Assuming modern-day passive upwelling rates as a minimum bound for Archaean upwelling rates, we estimate that a uniformly distributed layer of pure solidified liquid at the core–mantle boundary would be ~120–240 km thick (Methods). We also estimate that such a layer could account for 15–30% of the Earth's budget of incompatible trace elements.

The volume of dense melt generated between 10–22 GPa and trapped at the UM–TZ interface would be more than sufficient to account for the volume ($2 \pm 0.3\%$) of the two seismologically resolved and chemically distinct reservoirs in the lowermost mantle beneath the Pacific Ocean and Africa[27]. Thus, it is tempting to associate the material comprising these 'chemical piles' with a Fe-rich chemical boundary
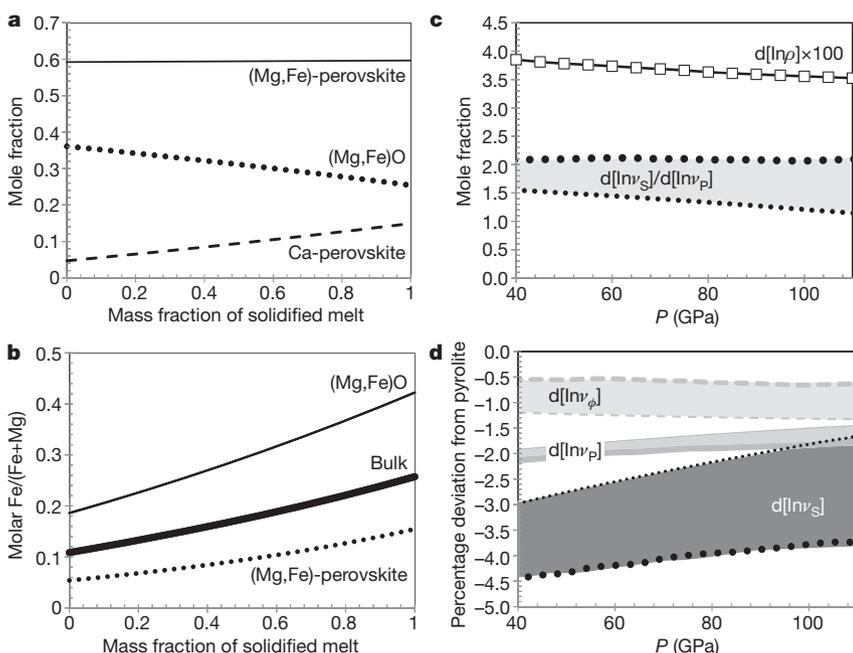

Figure 4 | Geophysical properties of Fe-rich chemical boundary layer. The physical properties of crystallized 14 GPa ultramafic liquids[16] at lower-mantle pressures. **a**, Phase proportions in mol.% in the lower mantle as a function of mass fraction of solidified ultramafic liquid. (Mg,Fe)O = ferropericlase. **b**, Molar Fe/(Fe+Mg) in bulk rock and mineral phases in the lower mantle (see Methods). **c**, Density of solidified melt as a function of pressure: percentage deviation from pyrolite, $d[\ln\rho] \times 100$. The ratio of relative deviations in shear and compressional velocities is $d[\ln v_S]/d[\ln v_P]$. **d**, Relative percentage deviations in shear ($d[\ln v_S]$), compressional ($d[\ln v_P]$) and bulk sound velocities ($d[\ln v_\phi]$) from pyrolite as a function of P. Calculations for pyrolite and crystallized melt in **c** and **d** assume 1,627 °C at the 660 km discontinuity. The bounds on the bands result from different shear moduli used for Ca-perovskite: high shear moduli[29] give higher v_S and v_P and lower v_ϕ (thinner lines) and lower shear moduli[31] give the opposite trends (thicker lines).

layer formed from these trapped liquids. These dense liquids have lower (Fe+Mg+Ca)/Si ratios and high Fe and Ca contents compared to their peridotite sources[16]. In the deep mantle, lithologies having this composition will have higher Fe (molar Fe/(Fe+Mg) ≈ 0.2), higher total perovskite (Ca-perovskite and (Mg,Fe)-perovskite), and lower ferropericlase ((Fe,Mg)O) content than a peridotite composition (Fig. 4a,b)[28] and will thus have distinct physical properties[29]. For example, the increased bulk Fe results in a 4% positive density anomaly (Fig. 4c). We expect Fe-enrichment to decrease shear modulus and hence shear velocity v_S). We also expect average bulk modulus to be influenced by phase proportions. Mg- and Ca-perovskite both have higher bulk moduli than ferropericlase, so in the case of compressional velocity v_P, an increase in perovskite mode would counterbalance the effect of increasing Fe content. Thus, variations in v_P and v_S could differ from those associated with thermal anomalies alone[27,30]. In detail, however, actual estimates of seismic velocities at lower-mantle conditions are limited by uncertainties in elastic parameters, particularly for Ca-perovskite, for which there is still debate over the value of its shear modulus and pressure derivative[29,31]. Given these uncertainties, possible ranges relative to peridotitic mantle are given in Fig. 4c and d: density increases by 4% (d[lnρ]), v_S decreases by 2–4% (d[lnv_S]), and v_P and bulk sound velocity (v_ϕ) decrease only slightly (d[lnv_P] = −2% and d[lnv_ϕ] = −0.5 to −1%). These calculations will undoubtedly evolve as our knowledge of elastic parameters at lower mantle conditions improves, but our predicted lithological compositions will not change much (Fig. 4a, b).

In summary, a necessary by-product of whole-mantle convection in a hot Archaean Earth is the generation of dense melts, which in turn generated Fe-rich hybrid layers at the UM–TZ interface. Sinking of these layers generates a deep mantle component with 'primordial' trace-element and noble gas isotopic signatures, providing an elegant explanation for the ubiquitous FOZO geochemical component in the mantle. However, in terms of major elements, these dense, high-pressure melts will not preserve the bulk silicate Earth composition. Estimates of the bulk silicate Earth composition, which are based on shallow-mantle samples, are thus biased if segregation of high-pressure melts occurred.

METHODS SUMMARY

Temperatures and pressures were calculated following the approach of ref. 22. Densities of liquids were calculated using a Birch–Murnaghan equation of state and parameters given in refs 17 and 18. Densities and elastic properties of solidified liquid in the lower mantle were calculated from mineral modes (estimated in two ways: minimization of the Gibbs free energy and mass action laws coupled with stoichiometric assumptions) and elastic properties extrapolated to elevated temperature and pressure[28,29].

Full Methods and any associated references are available in the online version of the paper at www.nature.com/nature.

1. Abe, Y. Thermal and chemical evolution of the terrestrial magma ocean. *Phys. Earth Planet. Inter.* **100**, 27–39 (1997).
2. Hofmann, A. W. Chemical differentiation of the Earth: the relationship between mantle, continental crust, and oceanic crust. *Earth Planet. Sci. Lett.* **90**, 297–314 (1988).
3. Kellogg, L. H., Hager, B. H. & van der Hilst, R. D. Compositional stratification in the deep mantle. *Science* **283**, 1881–1884 (1999).
4. Becker, T. W., Kellog, J. B. & O'Connell, R. J. Thermal constraints on the survival of primitive blobs in the lower mantle. *Earth Planet. Sci. Lett.* **171**, 351–365 (1999).
5. Tackley, P. J. Self-consistent generation of tectonic plates in three-dimensional mantle convection. *Earth Planet. Sci. Lett.* **157**, 9–22 (1998).
6. Class, C. & Goldstein, S. L. Evolution of helium isotopes in the Earth's mantle. *Nature* **436**, 1107–1112 (2005).
7. Kurz, M. D., Jenkins, W. J. & Hart, S. R. Helium isotopic systematics of ocean islands and mantle heterogeneity. *Nature* **297**, 43–46 (1982).
8. Graham, D. W. Noble gas isotope geochemistry of mid-ocean ridge and ocean island basalts: characterization of mantle source reservoirs. *Rev. Mineral.* **47**, 247–317 (2002).
9. van der Hilst, R., Widiyantoro, S. & Engdahl, E. R. Evidence for deep mantle circulation from global tomography. *Nature* **386**, 578–584 (1997).
10. Boyet, M. & Carlson, R. W. ¹⁴²Nd evidence for early (>4.53) global differentiation of the silicate Earth. *Science* **309**, 576–581 (2005).
11. Stixrude, L., de Koker, N., Sun, N., Mookherjee, M. & Karki, B. B. Thermodynamics of silicate liquids in the deep Earth. *Earth Planet. Sci. Lett.* **278**, 226–232 (2009).
12. Christensen, U. R. & Hofmann, A. W. Segregation of subducted oceanic crust in the convecting mantle. *J. Geophys. Res.* **99**, 19867–19884 (1994).
13. Miller, G. H., Stolper, E. M. & Ahrens, T. J. The equation of state of a molten komatiite. 2. Application to komatiite petrogenesis and the Hadean mantle. *J. Geophys. Res.* **96**, 11849–11864 (1991).
14. Stolper, E., Walker, D., Hager, B. H. & Hays, J. F. Melt segregation from partially molten source regions: the importance of melt density and source region size. *J. Geophys. Res.* **86**, 6261–6271 (1981).
15. Suzuki, A., Ohtani, E. & Kato, T. Density and thermal expansion of a peridotite melt at high pressure. *Phys. Earth Planet. Inter.* **107**, 53–61 (1998).
16. Herzberg, C. & Zhang, J. Melting experiments on anhydrous peridotite KLB-1: compositions of magmas in the upper mantle and transition zone. *J. Geophys. Res.* **101**, 8271–8295 (1996).
17. Lange, R. A. & Carmichael, I. S. E. Densities of Na₂O-K₂O-CaO-MgO-FeO-Fe₂O₃-Al₂O₃-TiO₂-SiO₂ liquids: new measurements and derived partial molar properties. *Geochim. Cosmochim. Acta* **51**, 2931–2946 (1987).
18. Ohtani, E. & Maeda, M. Density of basaltic melt at high pressure and stability of the melt at the base of the lower mantle. *Earth Planet. Sci. Lett.* **193**, 69–75 (2001).
19. Dziewonski, A. & Anderson, D. L. Preliminary reference earth model. *Phys. Earth Planet. Inter.* **25**, 297–356 (1981).
20. Tronnes, R. G. & Frost, D. J. Peridotite melting and mineral-melt partitioning of major and minor elements at 22–24.5 GPa. *Earth Planet. Sci. Lett.* **197**, 117–131 (2002).
21. Putirka, K. D., Perfit, M., Ryerson, F. J. & Jackson, M. G. Ambient and excess mantle temperatures, olivine thermometry, and active vs. passive upwelling. *Chem. Geol.* **241**, 177–206 (2007).
22. Lee, C.-T. A., Luffi, P., Plank, T., Dalton, H. A. & Leeman, W. P. Constraints on the depths and temperatures of basaltic magma generation on Earth and other terrestrial planets using new thermobarometers for mafic magmas. *Earth Planet. Sci. Lett.* **279**, 20–33 (2009).
23. Richter, F. M. Models for the Archean thermal regime. *Earth Planet. Sci. Lett.* **73**, 350–360 (1985).
24. Korenaga, J. Urey ratio and the structure and evolution of Earth's mantle. *Rev. Geophys.* **46**, doi:10.1029/2007RG000241 (2008).
25. Labrosse, S. & Jaupart, C. Thermal evolution of the Earth: secular changes and fluctuations of plate characteristics. *Earth Planet. Sci. Lett.* **260**, 465–481 (2007).
26. Hart, S. R., Hauri, E. H., Oschmann, L. A. & Whitehead, J. A. Mantle plumes and entrainment: isotopic evidence. *Science* **256**, 517–520 (1992).
27. Hernlund, J. W. & Houser, C. On the distribution of seismic velocities in Earth's deep mantle. *Earth Planet. Sci. Lett.* **265**, 423–437 (2008).
28. Mattern, E., Matas, J., Ricard, Y. & Bass, J. Lower mantle composition and temperature from mineral physics and thermodynamic modelling. *Geophys. J. Int.* **160**, 973–990 (2005).
29. Stixrude, L. & Lithgow-Bertelloni, C. Thermodynamics of mantle minerals—I. Physical properties. *Geophys. J. Int.* **162**, 610–632 (2005).
30. Ishii, M. & Tromp, J. Even-degree lateral variations in the Earth's mantle constrained by free oscillations and the free-air gravity anomaly. *Geophys. J. Int.* **145**, 77–96 (2001).
31. Li, L. *et al.* Elasticity of CaSiO3 perovskite at high pressure and high temperature. *Phys. Earth Planet. Inter.* **155**, 249–259 (2006).
32. Workman, R. K. & Hart, S. R. Major and trace element composition of the depleted MORB mantle (DMM). *Earth Planet. Sci. Lett.* **231**, 53–72 (2005).

Author Contributions C.-T.A.L. planned the paper, performed the modelling and wrote the paper; P.L. helped with the modelling and interpretation and figures; T.H. helped with the geodynamic interpretation; J.L. helped with the density modelling and interpretation; R.D. helped with the petrologic and geochemical interpretations; and J.H. helped with the geodynamic and mineral physics interpretations.

METHODS

Magma thermobarometry. The Earth's thermal history provides a key constraint on whether deep melting ever occurred. Parameterized convection models give qualitative insight[23–25]. A more direct approach is to estimate the temperatures and pressures of the mantle source regions giving rise to Archaean (>2.5 Gyr old) komatiites, ultramafic magmas inferred to be 40–50% partial melts of a dry fertile mantle source[16,33]. These estimated melt fractions are much larger than those generated under modern mid-ocean ridges (6–10%)[32,34] and suggest higher temperatures and initial pressures of melting in the Archaean era. Temperatures, based on the Mg content of the komatiites, indicate melting temperatures of at least 1,600–1,700 °C (refs 16 and 35), but there are no direct estimates of pressure.

We refine here the temperature estimates and provide constraints on the depths of melting using a barometer based on melt silica activity[21,22]. Temperatures and pressures of melting were calculated for primary magma compositions inferred by correcting for the effects of low-pressure fractional crystallization. Extensive details and principles of magma barometry are presented in ref. 22. Visual Basic code for olivine fractionation correction and P–T calculations are available upon request from C.-T.A.L. or direct download from the journal website[22]. In brief, magmas were corrected for olivine fractionation until a forsterite content (Mg/(Mg+Fe) × 100) of 91 for olivine was attained. In most cases, these minimal to no fractionation corrections were necessary because of the already very primitive nature of these komatiite compositions: that is, many appear to be near-primary mantle melts. Temperatures and pressures of equilibration of these primary magmas were then calculated.

We examined Archaean komatiites (>2.5 Gyr old) from the South African craton, West Australian craton, and Superior province in the Canadian shield (GEOROC data, http://georoc.mpch-mainz.gwdg.de). This data set includes the oldest (3.5 Gyr old) komatiites from the Barberton greenstone belt in South Africa. Assuming anhydrous conditions, komatiite P–T plots show a supersolidus array extending from 1,500 °C at 1.5 GPa (~45 km) to 1,750 °C at 7 GPa (~210 km) (Fig. 1). The array is oblique to that of the anhydrous lherzolite solidus and approximates a possible P–T path of partial melting. Extrapolation of the P–T trend to depth yields an intersection with the dry solidus at 8 GPa (240 km) and 1,800 °C; this intersection corresponds to a potential temperature of at least 1,700 °C. For higher potential temperatures, the initial depths of melting must therefore have been greater than ~240 km (Fig. 1). We note that ref. 36 argue that komatiites were wet, and as a consequence, their liquidus temperatures are <1,500–1,600 °C, only 200 °C hotter than the MORB source and within error of modern hotspot source regions like Hawaii. However, very low ferric to ferrous iron ratios in komatiite melt inclusions suggest that komatiites were dry[33]. In any case, water increases silica activity so that accounting for water decreases calculated temperatures and increases pressures (water depresses the solidus; see ref. 22 for discussion), so our pressures are minimum bounds.

Density calculations for liquids and solids in the upper mantle. Densities of liquids at increased temperature and pressure (up to 24 GPa) were calculated by first integrating with respect to temperature at a constant reference pressure P_0 (1 bar) and then integrating with respect to pressure at the elevated temperature T of interest. We followed the procedures of refs 15 and 37. The temperature integration followed:

$$\ln \frac{\rho(T_0, P_0)}{\rho(T, P_0)} = \int_{T_0}^{T} \alpha(T) \mathrm{d}T \tag{1}$$

where T_0 is the reference temperature (298.15 K for solids, but for a liquid, it is typically some temperature at which the liquid density was experimentally determined), ρ is density (kg m^{-3}), and α is the thermal expansivity (°C^{-1}). We used the following form of the thermal expansivity:

$$\alpha = \alpha_0 + \alpha_1 T + \alpha_2 T^{-1} + \alpha_3 T^{-2} \tag{2}$$

where the α_i are constants. After the density at elevated temperature was calculated, the density at elevated pressure was calculated using the third-order Birch–Murnaghan equation of state:

$$P = \frac{3}{2} K_T \left\{ \left(\frac{\rho}{\rho_0} \right)^{7/3} - \left(\frac{\rho}{\rho_0} \right)^{5/3} \right\} \left\{ 1 - \frac{3}{4} (4 - K') \left[\left(\frac{\rho}{\rho_0} \right)^{2/3} - 1 \right] \right\} \tag{3}$$

where P is pressure (GPa), K_T is the isothermal bulk modulus (GPa) at the temperature of interest, K' is the pressure-derivative (GPa/GPa) of the bulk modulus (assumed to be relatively temperature-independent), and $\rho_0 = \rho(T, P_0)$ is the reference pressure at the temperature of interest. The isothermal bulk modulus K_T at the temperature of interest is:

$$\ln \frac{K_T(T)}{K_T(T_0)} = - \int_{T_0}^{T} \alpha(T) \delta_T \mathrm{d}T \tag{4}$$

where δ_T is assumed to be a dimensionless constant that expresses the temperature dependency of elastic moduli. We assume that $\delta_T \approx K'$. Density at elevated pressure and temperature was then calculated by iteratively solving equations (1) to (4).

Densities of liquids at the reference temperature T_{ref} and 1 bar, $\rho_0 = \rho(T_0, P_0)$, for different compositions were calculated using the formulations of ref. 17:

$$V(T_r) = \sum X_i(T) \overline{V}_i(T_r) + X_{Na_2O} X_{TiO_2} \overline{V}_{Na_2O\text{-}TiO_2} \tag{5}$$

where X_i is the oxide mole fraction, $\overline{V}_i(T_r)$ is the molar volume of each oxide species at T_{ref}, and $\overline{V}_{Na_2O\text{-}TiO_2}$ is an effective molar volume for the Na$_2$O–TiO$_2$ interaction (see ref. 17 for parameter values). Liquid densities at elevated pressures were calculated using equation (3). Isothermal bulk moduli K_T and the pressure derivative K' were taken from refs 18 and 38. Following these[18,38], we adopted a maximum K' of 5. Liquid densities were calculated for peridotite partial melts (from solidus melts to liquidus melts) from the KLB-1 melting experiments of ref. 16. We applied our calculation methods to the liquid compositions of refs 18 and 38 and reproduced their results exactly, verifying the accuracy of our program. All of the above calculations were done in Visual Basic Excel (coded by C.-T.A.L.). The macro programs are available from C.-T.A.L. on request.

We did not consider the effects of water on density because high melt fractions are expected in these high-pressure melts, so water contents of the melt would be low; in addition, recent studies show that even in the presence of moderate amounts of water (<2 wt%), liquids still remain negatively buoyant[39,40].

Estimating total mass of 'sunken liquids'. This section concerns how much of this material may have formed and how much of the Earth's geochemical budget resides in this chemical boundary layer. Assuming whole-mantle convection, the present-day mass flow associated with passive upwelling (for example, the response to subduction) through the transition zone is 1.3×10^{24} kg per Gyr (assuming 10 cm yr^{-1} for full ridge spreading rate, 40,000 km total ridge length, ~100 km for the average thickness of subducting oceanic lithosphere, and a mantle density of 3,350 kg m^{-3}). This flow rate is a minimum bound because upwelling rates were probably higher in the Archaean era. Assuming that Archaean upwelling mantle melted by 10–20% above or within the transition zone and that such upwelling took place over the Earth's first billion years, at least $(1.3–2.6) \times 10^{23}$ kg of melt could have formed and sunk without ever reaching the Earth's surface. Spread uniformly around the core–mantle boundary, this would correspond to a layer ~120–240 km thick. If, as seems likely, the Fe-rich liquids are mixed in with peridotite before accumulating at the bottom of the mantle, the effective thickness of this chemical boundary layer will be greater.

The proportion of the Earth's incompatible trace element budget that could have been sequestered in this manner is then estimated from the concentration in the sunken liquid, which we take to be elevated by a factor of $1/f$, where f is the melting degree. If $f \approx 10$–20% (using a lower f would increase concentrations), the integrated mass of sunken liquids could make up 15–30% of the Earth's budget of incompatible trace elements. This number could be smaller if the window of time for generating negatively buoyant liquids is less than a billion years or larger if background upwelling rates were higher than assumed here. Our proposed Fe-rich chemical boundary layer has the geochemical characteristics of an undegassed and primordial mantle despite an origin by partial melting during whole-mantle convection and thus can solve many of the problems in mantle geochemistry.

Seismic velocities and densities of lower-mantle mixtures. Densities and seismic velocities at lower-mantle pressures were calculated following the approach of ref. 29 with a Fortran code written by G. Masters. Phase equilibria were calculated by assuming that the dominant cations are Ca, Mg, Fe and Si. Then, mole per cent Ca-perovskite (CaSiO$_3$) equals mole per cent Ca, (Mg,Fe)-perovskite, which equals the amount of Si not bound up in Ca-perovskite, and ferropericlase makes up the remaining phase. Mg and Fe are distributed between (Mg,Fe)-perovskite and ferropericlase according to an equilibrium constant $K_D^{Fe/Mg} = (Fe/Mg)_{perovskite}/(Fe/Mg)_{ferropericlase}$ between perovskite and ferropericlase of 0.25, from ref. 28. We ignored the effects of T and P on K_D. We also ignored the effect of Al in stabilizing (Mg,Fe)-perovskite because the amount of Al is small. The effect of Al on the $K_D^{Fe/Mg}$, however, could result in K_D approaching 1, such that the Fe/(Fe + Mg) ratio in Mg-perovskite and ferropericlase are the same. Accounting for Al, T and P could change our results slightly, but given the uncertainties in most of the elastic constants as well as in how K_D varies with Al, T and P, the first-order results presented here using a constant K_D are probably robust.

Isotropic adiabatic bulk and shear moduli (K_S and G) were determined from third-order expressions of the Eulerian finite strain. These calculations required input values of the molar volume, isothermal bulk and shear moduli, their pressure derivatives, the Debye temperature, the first and second logarithmic volume derivatives of the Debye temperature, and the shear strain derivative of the first derivative of the Debye temperature. These quantities were taken from ref. 29. For Ca-perovskite, we explored two parameter sets for shear modulus and

its pressure derivative, one from ref. 29 and the other from ref. 31. Linear mixing between the elastic moduli and molar volumes of endmember compositions was assumed (for example, MgO, FeO, $MgSiO_3$, $FeSiO_3$). The density and velocities of the aggregate lithology are determined by Voigt–Reuss–Hill averaging, using the phase proportions calculated above.

We calculated velocities and phase equilibria for pyrolite and solidified melt corresponding to an adiabat that intersects the 660 km discontinuity at 1,900 K. Because we are examining the simplified (Ca, Mg, Fe, Si) system we do not compare our calculations directly to PREM. We are primarily interested in the relative changes in seismic parameters caused by adding solidified melts to pyrolite. Therefore, in Fig. 4 of the main text, velocity perturbations are given with respect to our own calculations of simplified pyrolite (our pyrolite calculations are within 1% of PREM). We find the following systematics. Increasing net Fe content should substantially increase net density, but decrease net seismic velocities because perovskite and ferropericlase G decrease with increasing Fe/(Fe+Mg). Adding Si increases the proportion of perovskite phases, resulting in a slight decrease in net density and an increase in velocities. Because the addition of melt results in a net increase in Fe but an increase in perovskite proportion (balanced by a decrease in ferropericlase proportion), our calculations show that density increases substantially (controlled primarily by Fe), shear velocity decreases substantially (controlled primarily by Fe), and compressional and bulk sound velocities decrease only slightly (the latter are controlled by the perovskite/ferropericlase mode). The perturbations of shear, compressional and bulk sound velocities should be slightly decoupled from that expected from temperature variations or bulk Fe-content variations alone. However, we note that depending on the choice of shear moduli for Ca-perovskite, our results will be slightly different. Using the parameters of ref. 31, we find that the presence of Ca-perovskite does not affect shear velocity; consequently shear velocity of the solidified melt remains low due to the high bulk Fe content. If we use the parameters of ref. 29, which gives a higher shear modulus and pressure derivative for Ca-perovskite, the decrease in shear-wave velocity is less pronounced (and at lowermost mantle pressures, shear velocity actually increases beyond that of the pyrolitic mantle). Given that the elastic parameters for Ca-perovskite are still debated, it is probably not worth dwelling on these differences.

We emphasize that these velocity calculations are only as good as the elastic parameters adopted. Because these elastic parameters at lower mantle conditions are still a subject of debate, the details of our calculations could change. For example, if we were to adopt the higher shear modulus and pressure-derivative of Ca-perovskite[29], the shear-wave velocity of the solidified melt would increase rapidly with depth, resulting in less of a shear-wave velocity anomaly and giving a low $d[\ln V_S]/d[\ln V_P]$ of ~1.

Finally, calculations were also done for a more natural composition (that is, accounting for additional components, such as Al, Na and K) using Perplex, a Gibbs free energy minimization program that solves for phase proportions and compositions given a bulk composition and then calculates seismic velocities using procedures similar to those described above[41]. This program incorporates the thermodynamic and physical properties of lower-mantle minerals from ref. 29. These results were consistent with the simplified oxide system taken above.

33. Berry, A. J., Danyushevsky, L. V., O'Neill, H. S. C., Newville, M. & Sutton, S. R. Oxidation state of iron in komatiitic melt inclusions indicates hot Archaean mantle. *Nature* **455**, 960–964 (2008).

34. Langmuir, C., Klein, E. M. & Plank, T. (eds) *Petrological Systematics of Mid-Ocean Ridge Basalts: Constraints on Melt Generation Beneath Ocean Ridges* (American Geophysical Union, 1992).

35. Arndt, N. T. Komatiites, kimberlites and boninites. *J. Geophys. Res.* **108**, doi:10.1029/2002JB002157 (2003).

36. Grove, T. L. & Parman, S. W. Thermal evolution of the Earth as recorded by komatiites. *Earth Planet. Sci. Lett.* **219**, 173–187 (2004).

37. Bina, C. R. & Helffrich, G. R. Calculation of elastic properties from thermodynamic equation of state principles. *Annu. Rev. Earth Planet. Sci.* **20**, 527–552 (1992).

38. Ohtani, E., Kawabe, I., Moriyama, J. & Nagata, Y. Partitioning of elements between majorite garnet and melt implications for petrogenesis of komatiite. *Contrib. Mineral. Petrol.* **103**, 263–269 (1989).

39. Sakamaki, T., Suzuki, A. & Ohtani, E. Stability of hydrous melt at the base of the Earth's upper mantle. *Nature* **439**, 192–194 (2006).

40. Agee, C. B. Static compression of hydrous silicate melt and the effect of water on planetary differentiation. *Earth Planet. Sci. Lett.* **265**, 641–654 (2008).

41. Connolly, J. A. D. & Petrini, K. An automated strategy for calculation of phase diagram sections and retrieval of rock properties as a function of physical conditions. *J. Metamorph. Geol.* **20**, 697–708 (2002).